Lanthanum-Promoted Electrocatalyst for the Oxygen Evolution Reaction: Unique Catalyst or Oxide Deconstruction?

Alaina C. Hartnett, Ryan J. Evenson, Agnes E. Thorarinsdottir, Samuel S. Veroneau, and Daniel G. Nocera*

Department of Chemistry and Chemical Biology, Harvard University, 12 Oxford Street, Cambridge, MA 02138, United States

ABSTRACT: A conventional performance metric for electrocatalysts that promote the oxygen evolution reaction (OER) is the current density at a given overpotential. However, the assumption that increased current density at lower overpotentials indicates superior catalyst design is precarious for OER catalysts in the working environment, as the crystalline lattice is prone to deconstruction and amorphization, thus greatly increasing the concentration of catalytic active sites. We show this to be the case for La^{3+} incorporation into Co_3O_4. Powder X-ray diffraction (PXRD), Raman spectroscopy and extended X-ray absorption fine structure (EXAFS) reveal smaller domain sizes with decreased long-range order and increased amorphization for La-modified Co_3O_4. This lattice deconstruction is exacerbated under the conditions of OER as indicated by operando spectroscopies. The overpotential for OER decreases with increasing La^{3+} concentration, with maximum activity achieved at 17% La incorporation. HRTEM images and electron diffraction patterns clearly show the formation of an amorphous overlayer with OER catalysis that is accelerated with La^{3+} addition. O 1s XPS spectra after OER show the loss of lattice-oxide and an increase in peak density associated with hydroxylated or defective regimes, consistent with $Co(O)_x(OH)_y$ species in an amorphous overlayer. Our results suggest that improved catalytic activity of oxides incorporated with La^{3+} ions (and likely other metal ions), generally ascribed to enhanced intrinsic catalysis, is due to an increase in the number of terminal octahedral $Co(O)_x(OH)_y$ edge sites upon Co_3O_4 lattice deconstruction, rather than enhanced intrinsic catalysis.

INTRODUCTION

Water splitting catalysis underpins all sustainable energy conversion schemes as the reaction is the source of proton and electron reducing equivalents, whether they are used for green hydrogen generation or for driving small molecule reduction reactions, the most popular of which is the reduction of CO_2 to fuels.[1−4] The anodic half-reaction of water splitting—the oxygen evolution reaction (OER)—is the most kinetically demanding as two water molecules must be coupled to produce oxygen governed by a four-equivalent, proton-coupled electron transfer mechanism.[5−7] Materials and chemical synthesis has delivered scores of OER catalysts over the past decade.[8] Of these, mixed-metal oxides are particularly attractive catalyst targets as they often exhibit increased OER activity.[9−11] The origin of this enhanced OER activity of mixed-metal oxides has been ascribed to several factors, including: (1) optimized metal–oxygen covalency and resulting favorable intermediate energetics,[12−17] (2) strain and defect-induced reactivity enhancements,[18−24] (3) favorable entropic contributions to the water splitting reaction[25,26] and (4) Lewis-acid promoted proton-coupled electron transfer (PCET).[27,28] Introduction of Ln^{3+} (Ln = lanthanide) ions to first-row transition metal oxides has recently appeared as an effective strategy to enhance water splitting.[12,29−37] The large ionic radius of Ln^{3+} ions compared to those of first-row transition metals has been proposed to increase the likelihood of unique structural modifications to the oxide lattice. Indeed, La^{3+} has been shown to enhance OER catalysis of Co_3O_4 in acidic conditions and the La-Co_3O_4 system has been utilized as potential anode in a PEM electrolyzer.[31]

In the simplest formulation, the current density for OER catalysis (j_{OER}) is defined as,[38−40]

$$j_{OER} = 4Fk_{OER}{}^{0}C_{as}{}^{*}\exp(\alpha\eta F/RT) \quad (1)$$

is determined by the intrinsic catalytic rate ($k_{OER}{}^{0}$, defined by the exchange current density), the overpotential for the OER (η) and the concentration of catalytic active sites ($C_{as}{}^{*}$). Other parameters in eq (1) are the Faraday constant (F), the gas constant (R), the reaction temperature (T), and the charge transfer coefficient (a). Performance metrics for the OER often report the current density at a given overpotential, and an increased current at lower overpotential is ascribed to superior catalyst design, i.e., enhanced $k_{OER}{}^{0}$. However, this assumption of an intrinsically "better" catalyst in the working environment is tenuous at best as a higher current density at a lower overpotential may instead be due to a higher concentration of active sites. This assumption in catalyst performance is especially problematic if the crystalline lattice of the OER catalyst in the working environment is prone to deconstruction and amorphization. For instance, one of the simplest unary metal oxides, Co_3O_4, has long been thought to be a superior OER catalyst.[41,42] In its pristine form, Co_3O_4 assumes a normal spinel lattice with divalent Co^{2+} ions residing in tetrahedral sites and trivalent Co^{3+} ions residing in octahedral sites of the cubic closed packed oxide lattice. However, high-resolution transmission electron microscopy (HRTEM) studies of crystalline cobalt oxides, such as $LiCoO_2$ and Co_3O_4, under the conditions of OER reveal that the surface of the oxide is indeed an amorphous overlayer containing $CoO_x(OH)_y$ active sites.[43−46] For the case of mixed-metal oxygen

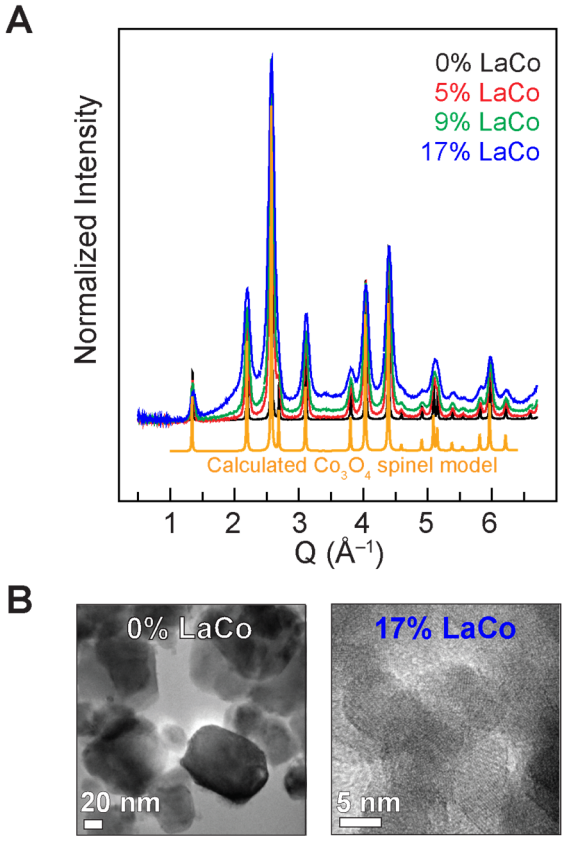

Figure 1. (A) High energy PXRD patterns of 0-17% LaCo films. (**B**) TEM images of polycrystalline films of 0% LaCo (left) and 17% LaCo (right).

evolving catalysts (MM′-OECs, e.g., M = Co or Ni, M′ = Ln^{3+}), it is crucial to understand the nature of M′ incorporation because a "more active" catalyst may not be due to enhanced catalytic activity (k_{OER}^0) but simply a result of more active sites (C_{as}*) arising from amorphization of the catalyst. We now show this to be the case for La^{3+} modified Co_3O_4. Ex situ and operando spectroscopies, and high-resolution imaging, reveal that La^{3+} deconstructs the Co_3O_4 crystalline surface to produce an amorphous overlayer with an increased concentration of $CoO_x(OH)_y$ active sites. Although optimized La^{3+} doping levels can stabilize the amorphous overlayer over short time periods (80–90 h), the overlayer ultimately dissolves. These results highlight the importance of understanding the nature of the active site in OER catalysts and, accordingly, the need to distinguish between intrinsic catalytic OER activity (k_{OER}^0 in eq (1)) as opposed to lattice deconstruction to furnish a greater active site concentration (C_{as}* in eq (1)) when reporting current density versus overpotential as a performance metric.

RESULTS

Lanthanum–Cobalt Oxide Catalyst Preparation. Cobalt–oxide (Co_3O_4) (denoted 0% LaCo) and La-incorporated cobalt–oxide catalysts (denoted 5–30% LaCo) were fabricated using a modified Pechini sol–gel procedure[47,48] (Figure S1) using cobalt(II) and lanthanum(III) nitrate precursor salts. Pre-cleaned fluorine-doped tin oxide (FTO) substrates were dip-coated in the sol–gel precursor solutions and annealed at 600 °C in air to form the pure and mixed metal–oxide catalyst films. La compositions were determined from inductively-coupled plasma mass spectrometry (ICP–MS) of digested films (Figure S2). La incorporation monotonically increased with the concentration of La introduced into the sol–gel precursor solution.

Structural Characterization of Prepared Films. Perturbation of the cobalt oxide lattice by La incorporation was examined with X-ray photoelectron spectroscopy (XPS). The Co 2p XPS spectra of LaCo films show two strong peaks with binding energies of 795 eV and 780 eV, along with a weak peak at 790 eV (Figure S3A). These features correspond to Co $2p_{1/2}$ and $2p_{3/2}$ peaks, and its associated satellite peak, consistent with the Co 2p binding energies of Co_3O_4.[49] The observation of two La $3d_{5/2}$ peaks in the XPS spectra of LaCo films establishes the oxidation state of La as trivalent (Figure S3B).[50] The spacing between La $3d_{5/2}$ peaks is chemically diagnostic of La speciation; spacings of 3.9 eV, 3.5 eV, and 4.6 eV are characteristic of spacing of $La(OH)_3$, $La_2(CO_3)_3$, and La_2O_3, respectively.[50,51] Our observation of an average spacing of 3.7 eV in La-modified samples (Figure 3SB) indicates that La^{3+}, at the surface of the oxide and in the presence of air and water, can assume a hydroxide and/or carbonate coordination environment, as the solubility products of $La(OH)_3$ and $La_2(CO_3)_3$ are very favorable ($K_{sp}(La(OH)_3 = 2 \times 10^{-19}$, $K_{sp}(La_2(CO_3)_3 = 4 \times 10^{-34}$).

The native Co_3O_4 (0% LaCo) and 5–17% LaCo samples prepared by the sol–gel method are polycrystalline. High-energy powder X-ray diffraction (PXRD) patterns were collected on 0–17% LaCo samples at the 17-BM beamline of the Advanced Photon Source at Argonne National Laboratory. Rietveld refinement of the PXRD pattern for as-prepared 0% LaCo precisely matches that of the Co_3O_4 spinel structure (Figure 1A)[52] with no evidence of $CoO(OH)$ or $Co(OH)_2$. Upon La incorporation, the PXRD peaks of the Co_3O_4 spinel structure broaden, indicating smaller particle sizes as La^{3+} infiltrates the Co_3O_4 lattice. Fits of 2D PXRD patterns with GSAS-2[53] by varying both domain size and isotropic micro-strain yielded domain sizes of 67, 16, 11, and 8 nm for 0, 5, 9, and 17% LaCo, respectively (Figure S4). The trend in domain size is consistent with HRTEM images of samples, which show decreased crystallite dimensions with increasing La incorporation (Figure 1B). This analysis is further supported by double layer capacitance (DLC) measurements utilized to determine the electrochemically active surface area (ESCA). By comparing the relative differences in capacitive current in a non-faradaic potential regime, we measure 11.5(4.9) times higher ECSA for 17% LaCo as compared to 0% LaCo (Figure S5). This increase in ECSA agrees well with the geometric dimensions of the different average particle sizes of 67 nm for 0% LaCo and 8 nm for 17% LaCo. Assuming the packing of spherical particles within a 400 nm thick catalyst layer (as measured by a cross-sectional scanning electron microscopy (SEM) image, Figure S6), an expected surface area of 17% LaCo is calculated, which is 8.4 times that of 0% LaCo. This increase in surface area agrees well with the relative ECSA of 11.5× measured by DLC. Importantly, the ECSA measured by DLC is likely convoluted by several factors in dynamic metal-oxide systems including ion adsorption, intercalation, and conductivity decreases due to $Co(OH)_2$ formation, all of which can contribute to assumed capacitive current resulting in error.[54] For these reasons, ECSA measured by DLC cannot accurately reveal active site density.

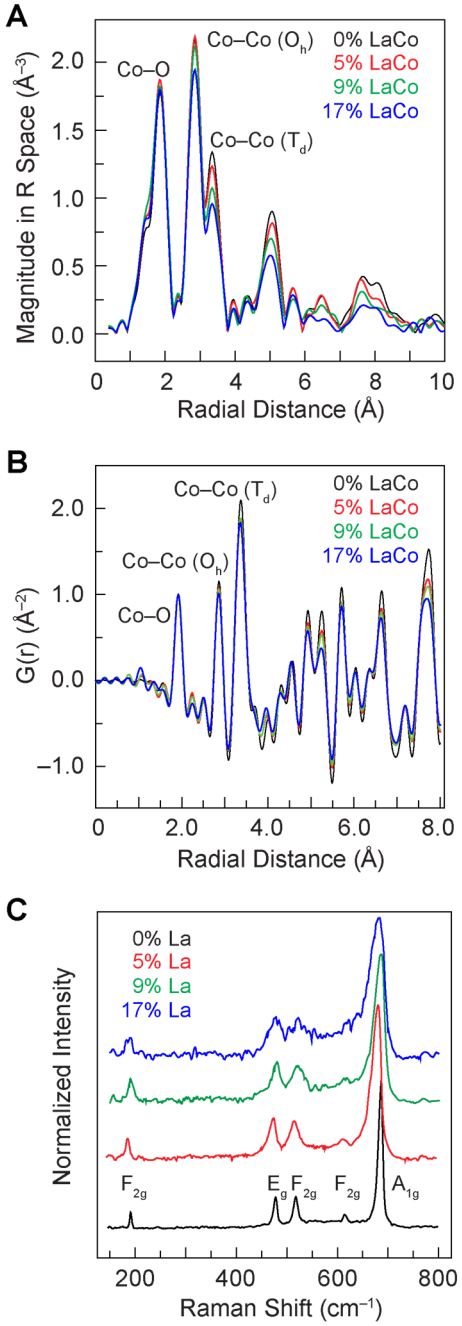

Figure 2. Structural characterization of as synthesized 0–17% LaCo films. (**A**) Co K-edge EXAFS spectra and (**B**) PDF analysis of total X-ray scattering data. Selected interatomic distances are labelled, see Figure S7 for assignment of other distances in EXAFS and PDF spectra. (**C**) Raman spectra of %LaCo films referenced to that of Co_3O_4.

Extended X-ray absorption fine structure (EXAFS) and X-ray pair distribution function (PDF) analyses of as-synthesized LaCo films reveal loss of structural order as a function of increasing La composition. The EXAFS spectra at the Co K-edge, shown in Figure 2A, display radial distances in Co_3O_4 that do not significantly shift with %La incorporation, but peak intensity decreases are evident at all radial distances. Figure S7 lists the Co–O bond lengths and various Co···Co distances determined from the EXAFS spectra as compared to those of Co_3O_4. La incorporation disproportionately affects T_d Co sites, with larger decreases in intensity occurring at 3.35 Å ($O_h \cdots T_d$ distance) as compared to 2.87 Å ($O_h \cdots O_h$ distance). Decreases in peak intensities are also evident at all larger radial distances, most notably those corresponding to $Co^{3+}(O_h)$ in cubane–cubane subunits at 5.06 Å and at all $Co(O_h)$ cubane–$Co(T_d)$ distances. Similar to the EXAFS spectrum, the Co–O distance (1.89 Å) calculated by PDF analysis of total X-ray scattering data is not affected with La^{3+} concentration, however, as observed in EXAFS, there is a loss of both general and site-specific structural coherence for all peaks between 2.0 and 8.0 Å (Figure 2B), with the largest intensity decreases observed for radial distances corresponding to all $Co(O_h)$ cubane–$Co(T_d)$ sites (5.25 Å and 7.76 Å). Whereas these structural metrics correspond to Co_3O_4 signatures (Figure S7), PDF analysis (Figure S8) clearly shows a distinct residual scattering signal at 3.3 Å that is unaccounted for by a Co_3O_4 spinel model. This La^{3+}-dependent signal is consistent with nearest neighbor La···Co distances that are observed in layered La cobaltates (3.235 Å, Figure S7).[55,56]

The Raman spectra shown in Figure 2C are consistent with X-ray and EXAFS structural studies. All Raman-active Co_3O_4 spinel modes can be resolved for 0% LaCo (A_{1g}: 689.4 cm^{-1}; F_{2g}: 616.9 cm^{-1}, 520.8 cm^{-1}, 194.1 cm^{-1}; E_g: 480.6 cm^{-1}).[57–59] The asymmetric peak broadening and shift to lower energy of the singly degenerate A_{1g} Raman mode is consistent with the phonon confinement model that becomes more prevalent as the crystallite size decreases.[60–62] For all Raman-active modes, increased peak broadening, shifting of peaks to lower energies, and decreases in signal intensity accompanies increased La incorporation, consistent with the loss of crystallinity and long-range order.

OER Activity of 0–17% LaCo Films. The cyclic voltammograms (Figure 3A) of 0–17% LaCo films in acidic solution (pH 2) are dominated by the $Co^{3+/2+}$ redox feature.[63] Gas chromatography verified that OER proceeded with 100% faradaic efficiency. Increased activity is reflected in the decreasing OER overpotential with increasing %La, with the lowest overpotential (Figure 3B) and exchange current density (Figure 3C) observed for the 17% LaCo catalyst. The OER mechanism does not appear to be affected by La^{3+} incorporation, as the Tafel slopes of all catalyst compositions are invariant (76–88 mV dec^{-1}). We note that for film compositions greater than 17% LaCo, the overpotential increases, indicative of a loss of catalytic activity (purple trace, Figure 3B). This instability may be observed directly with constant current experiments. Whereas a 0% LaCo film maintains its overpotential when operated at 1 mA cm^{-2} in an acidic environment (pH 2) for 45 h and a 17% LaCo film for nearly 80 h, a 30% film is stable for only 3 h with complete dissolution over the proceeding 3 h (Figure S9). Due to the solubility of Co^{2+} and La^{3+} in acid, Co and La leaching from the amorphous overlayer occurs over time at pH 2, as clearly detected by ICP–MS analysis (Table S1). ICP-MS reveals the highest leaching to occur during initial OER operation at 1 mA cm^{-2} for 17% LaCo (1.1 nM/min Co and 1.3 nM/min La) as the Co_3O_4 lattice is deconstructed to the amorphous overlayer.

Operando and Post-Catalysis Characterization. To better understand the effect of La^{3+} incorporation, operando Raman spectroscopy was performed in acidic solutions (pH 2) in a 3-electrode cell with a thin layer of electrolyte solution covering the electrode surface.[64] The anodic current was increased from 0.1–20 mA and then decreased over the same range in a stepwise manner.

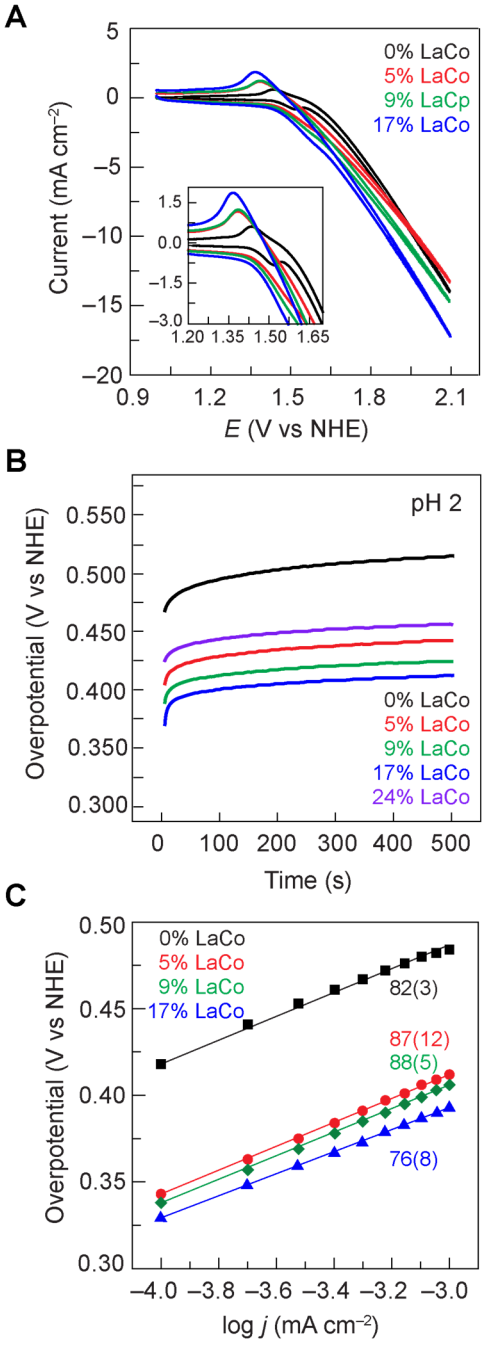

Figure 3. Electrochemical activity of 0–17% LaCo films. All measurements were carried out at pH 2 using 10 mM H_2SO_4 solutions containing 200 mM K_2SO_4 as supporting electrolyte. (**A**) Cyclic voltammogram collected at 100 mV s^{-1}: inset shows increasing cathodic current associated with the $Co^{3+/2+}$ redox feature with increasing La concentration. (**B**) Overpotential for OER at an anodic current density of 1 mA cm^{-2}. (**C**) OER Tafel slopes for 0–17% LaCo films. Errors in overpotential and Tafel slope were determined from measurements of three independent films

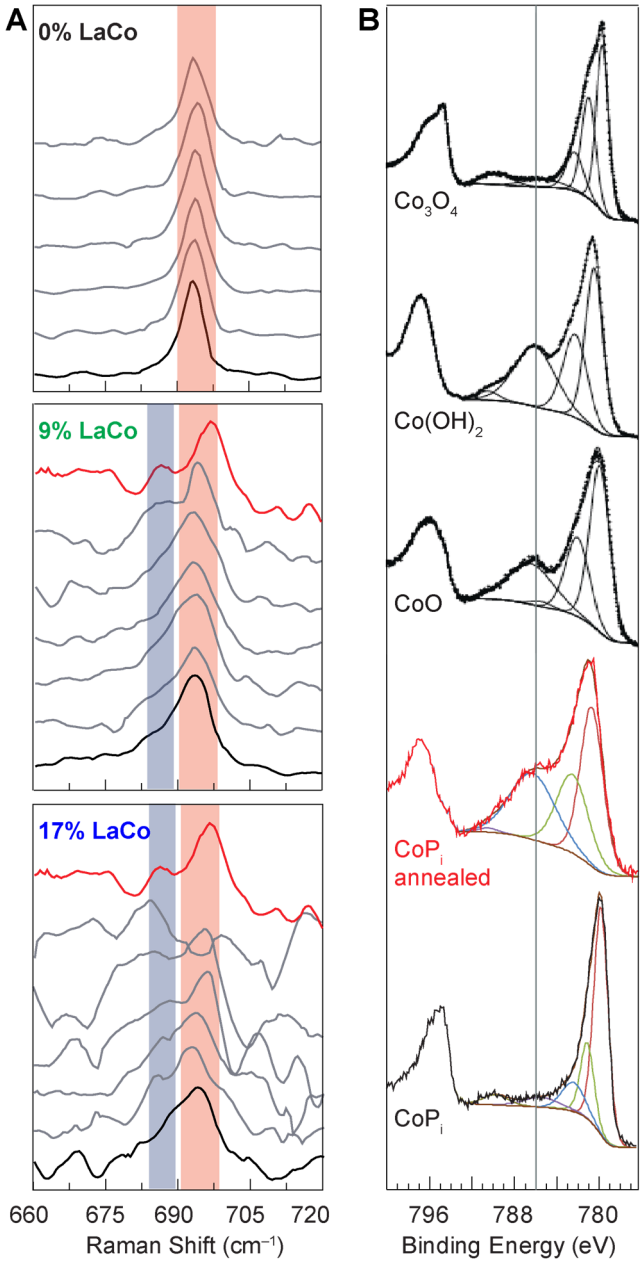

Figure 4. (**A**) Operando Raman spectra of 0 (top), 9 (middle), and 17% (bottom) LaCo films before applying a current (0 mA, black line) and *in situ* spectra recorded during the application of 0.1, 1, 5, 10 and 20 mA (gray traces, bottom to top) during OER. The current density was maintained at each step for 120 s. All spectra were taken of films operated in 10 mM H_2SO_4 containing 200 mM K_2SO_4 (pH 2). The pink bar highlights the A_{1g} Raman peak of Co_3O_4 and the blue bar highlights a unique feature that grows in with increased current. The red trace is the Raman spectrum of CoP_i annealed at 600 °C. (**B**) The Co $2p_{3/2}$ and Co $2p_{1/2}$ peaks in the XPS spectra of electrodeposited CoP_i, CoP_i annealed at 600 °C and reference Co oxide XPS spectra taken from ref 49. The grey line highlights the Co $2p_{3/2}$ satellite peak.

The Raman spectra shown in Figure 4A were recorded while maintaining the current at each step for 120 s. While the Raman spectrum in the spectral window of the A_{1g} peak (at ~693 cm^{-1} in Figure 4A, red bar highlight) for 0% LaCo remains unchanged during OER, a new feature (at ~684 cm^{-1} in Figure 4A, blue-gray bar highlight) emerges for the LaCo samples during OER operation. The appearance of this new feature is dependent on the applied current density and appears at lower current densities for catalysts with higher concentrations of La^{3+}. Upon returning to open circuit potential, this peak disappears, indicating that it is associated with the OER. The in-situ Raman peak can be reproduced in ex-situ

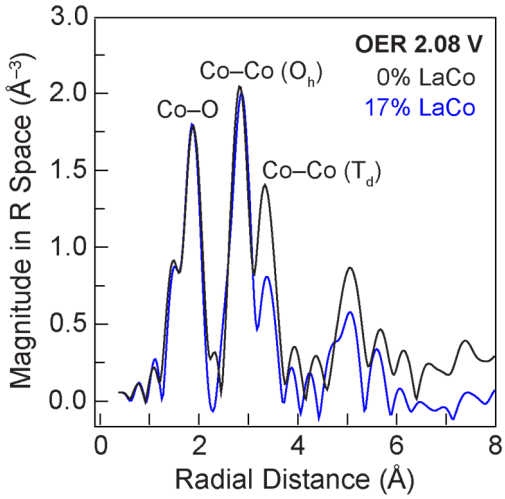

Figure 5. Operando Co K-edge EXAFS spectra of 0% LaCo and 17% LaCo films collected after 30 min of OER at 2.08 V vs NHE, at an anodic current density of 1 mA cm^{-2} in 10 mM H_2SO_4 containing 200 mM K_2SO_4 (pH 2).

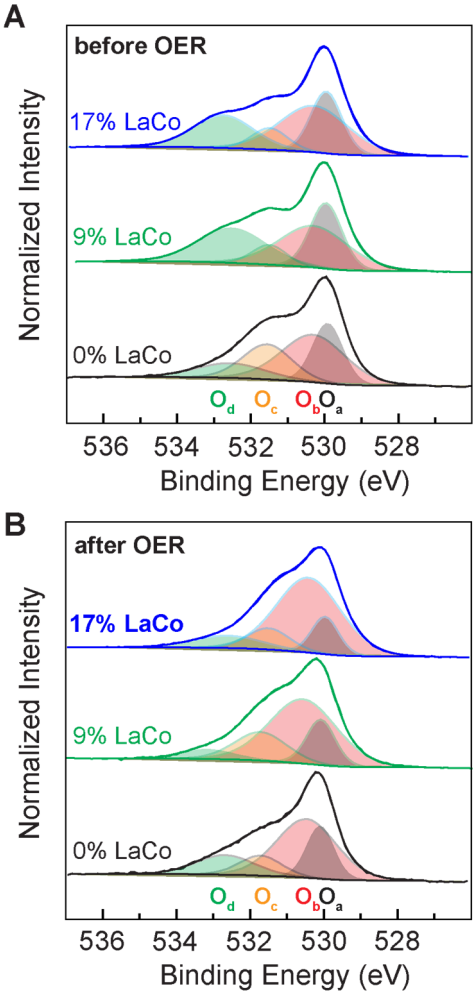

Figure 6. Deconvolved O 1s XPS spectra of 0–17% LaCo films before and after OER for 1 h at anodic current density of 1 mA cm^{-2} in 10 mM H_2SO_4 containing 200 mM K_2SO_4 (pH 2): O_a (gray, Co–O lattice), O_b (red, defect/hydroxylated O), O_c (orange, C–O), and O_d (green, C=O).

spectra of annealed samples of CoP_i (Figure 4A, red trace), indicating that the structural phase evolving in-situ for 17% LaCo is also present in annealed CoP_i.[65] The origin of the species responsible for the operando feature is revealed by Co 2p XPS spectra. Figure 4B shows the Co $2p_{3/2}$ absorption and its satellite deconvolved into five peaks, as previously described.[49] Whereas electrodeposited CoP_i possesses a Co 2p XPS spectrum similar to Co_3O_4, upon heating, the XPS spectrum of CoP_i transforms to a spectrum that clearly matches $CoO/Co(OH)_2$. The annealed CoP_i shows the appearance of a Raman peak at a vibrational frequency of 684 cm^{-1} (Figure 4A, red trace). This peak has been assigned to the A_{1g} mode of Co^{2+} residing in a O_h oxide environment.[66–68] Thus, the origin of the new Raman peak that appears in the operando spectra of LaCo samples is a result of the in-situ formation of Co^{2+} in octahedral sites during OER.

Operando EXAFS is consonant with the presence of increased catalyst disorder with La incorporation and provides additional insights regarding the evolution of the catalytically active phase. Operando EXAFS measurements were carried out in a 3-electrode electrochemical cell where the working electrodes were a 0–17% LaCo film dip-coated on X-ray transparent graphene substrates. The applied potential on the working electrode was varied in a stepwise manner, with EXAFS spectra collected at open circuit potential before OER catalysis, and at 2.08 V vs NHE during OER catalysis. Comparison of the EXAFS spectra collected during OER (Figure 5) reveals structural disorder that is more pronounced with increasing %La (Figure 5). The observed changes in the operando spectra are similar to those observed with increased %La prior to OER (Figure 2A) but more pronounced under an applied OER potential. Loss of long-range coordination and increased structural disorder is reflected by a decrease in peak intensity at 3.35 Å, indicating loss of T_d Co sites during OER. Additionally, a shoulder appears at 4.8 Å in the spectrum of the 17% LaCo catalyst and the peak at 5.6 Å increases in intensity, which coincides with the interlayer Co distances in the EXAFS spectrum of layered $LiCoO_2$[69] and the crystal structure of $La_{0.3}CoO_2$ (Table S6).[56] Thus, the changes in the Co EXAFS spectra of 17%LaCo suggest that the Co_3O_4 lattice is deconstructed by La^{3+} termination to form amorphous layered $CoO_x(OH)_y$ with La^{3+} residing at particle interfaces.

The O 1s XPS spectra shown in Figure 6 provide further evidence for irreversible changes dependent on catalyst composition. The O 1s XPS spectra of LaCo films includes peak contributions from oxygen atoms in the environments of: the cobalt-oxide lattice (O_a, Co–O, 530.0 eV), hydroxylated or defect-rich mixed-metal regions (O_b, 530.3 eV), C–O groups arising from adventitious surface carbon species (O_c, 531.5 eV) , and C=O (e.g., carbonate) surface species (O_d, 532.5 eV), all of which may be assessed by peak area fitting of the XPS spectra.[49,70] Before OER operation, the lattice cobalt–oxygen contribution (O_a) remains relatively constant, though slight broadening with increasing La concentration (FWHM 0.9 to 1.2 eV) indicates more lattice bonding variation. Prior to OER, La^{3+} promotes the formation of metal carbonate surface species as evidenced by the increased O_d 1s peak area. Subsequent to OER (pH 2, 1 mA cm^{-2} for 30 min), the O_b peak area increases significantly and monotonically with increasing %La with a concomitant decrease in O_a. This trend is consistent with amorphization of the Co_3O_4 lattice during OER.

Consistent with operando spectra, HRTEM images of a 17% LaCo taken before and after OER catalysis visually show the

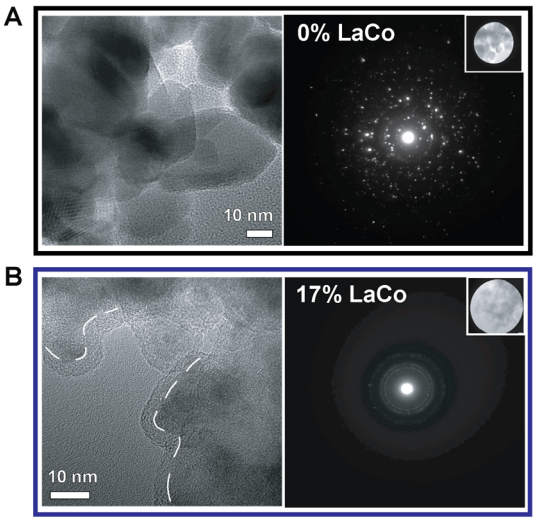

Figure 7. HRTEM images and selected area diffraction patterns of (**A**) 0% LaCo and (**B**)17% LaCo films after 10 h of OER operation at an anodic current density of 1 mA cm^{-2} in 10 mM H_2SO_4 solution containing 200 mM K_2SO_4. Overlayer on 17% LaCo is outlined by white dashed line.

irreversible deconstruction of the Co_3O_4 lattice. The selected area electron diffraction (SAED) patterns of 0% and 17% LaCo films clearly show the polycrystalline nature of the films before OER; this polycrystallinity significantly degrades after OER with the 17% LaCo film exhibiting almost a complete loss of a crystalline diffraction pattern (Figure S10). As shown in HRTEM images of Figure 7, the image of the 17% LaCo catalyst, which exhibits the highest OER activity (Figure 3), clearly shows the emergence of an amorphous overlayer, highlighted by the dashed line of the HRTEM image in Figure 7B. HRTEM images of 30% LaCo (Figure S10) reveal a well-defined amorphous overlayer that is present even before catalysis. This layer promptly dissolves under the conditions of OER (Figure S9).

DISCUSSION

Crystalline cobalt oxides under OER conditions have been observed to undergo in-situ deconstruction to catalytically active $CoO_x(OH)_y$ (i.e., CoO(OH) and $Co(OH)_2$) sites comprising an amorphous overlayer.[70–78] In the presence of specific anions such as phosphate or borate, the dimensional reduction of the crystalline cobalt or nickel oxides can be so extensive as to produce cobaltate and nickellate clusters of molecular dimensions.[79–82] Previous studies of OER at $CoO_x(OH)_y$ sites support the mechanisms outlined in Figure 8A. A $Co^{2+}{}_2$ edge site is oxidized to a $Co^{3+}Co^{4+}$ pre-catalysis. Localized at the edges, the Co^{4+} center may be considered to have significant Co^{3+}-oxyl radical character.[83,84] This radical character is a direct consequence of the electronic considerations embodied by the "oxo wall", which prevents multiple metal-oxo bond formation owing to filled $d\pi(d_{xz},d_{yz})$ orbitals.[85] X-ray absorption spectroscopy (XAS),[72,79,86,87] electron paramagnetic resonance spectroscopy,[63,88] and transient absorption spectroscopy[73] confirm that the pre-catalyst resides in a formal Co^{4+} redox level, though in macroscopic samples, the relative amounts of Co^{4+} to Co^{3+} is difficult to spectroscopically detect[89] because the concentration of the pre-catalyst is small relative to the total concentration of Co^{3+} together with the contribution of the Co^{3+}-oxyl resonance structure to the pre-catalytic resting state (Figure 8B); suffice is to say that the pre-equilibrium resting state is one redox level above Co^{3+}-oxo. Electrokinetics studies establish that a $Co^{4+}{}_2$ ($\leftrightarrow$ $(Co^{3+}\text{-oxyl})_2$) catalytic active site is generated from a $1e^-/1H^+$ PCET pre-equilibrium.[90] The rate-determining step is proposed to occur via a peroxide intermediate, which may form by direct coupling of oxyls,[91–94] attack by an oxyl on solution hydroxide,[91,95–97] or on a bridging (hydr)oxide (Figure 8B).[98–102] Upon O_2 formation, the active edge sites return to an octahedrally coordinated $Co^{2+}{}_2$ formal redox level. The benefit of a dimensional reduction of a Co_3O_4 lattice is that it generates $CoO_x(OH)_y$ active edge sites from which OER catalysis may proceed. Unlike in crystalline Co_3O_4 where the oxygen atoms are kinetically inert owing to their coordination to multiple cobalt centers, at a $CoO_x(OH)_y$ edge, oxygen is singly bonded to cobalt and thus is more kinetically labile to activation.

Due to the steric incompatibility of La^{3+} with the crystalline Co_3O_4 lattice, La^{3+} introduction accelerates the dimensional reduction of Co_3O_4 to an amorphous overlayer with an increased concentration of $CoO_x(OH)_y$ edge sites. The PXRD data shown in Figure 1 establishes a crystalline Co_3O_4 phase that becomes more amorphous with increasing %La. The loss of crystallinity is exacerbated by OER catalysis; HRTEM images of LaCo catalyst films (Figure 7) clearly show the formation of an amorphous overlayer with La^{3+} incorporation under OER conditions. At dopant levels in excess of 17%, the amorphous overlayer is present even prior to OER operation (Figure S10). The formation of the amorphous overlayer is accompanied by greater OER activity with the maximal activity observed for 17% LaCo (Figure 3). ICP–MS analyses of all film compositions for which the data were collected in Figure 3 reveals that the overall Co concentration is similar across the LaCo series; only the extent of amorphization varies with %La incorporation. These results are consistent with La^{3+} promoting Co_3O_4 deconstruction and the formation of $CoO_x(OH)_y$ active sites in an amorphous overlayer that coats crystalline Co_3O_4, which serves to transport hole equivalents to the active catalytic sites residing in the amorphous overlayer.

All spectral data indicate that the large La^{3+} ion is not substituting for Co sites within the Co_3O_4 lattice. EXAFS spectra reveal that the Co···Co and Co–O distances of LaCo films match those in Co_3O_4 (Figure 2A and Figure S7) indicating that La^{3+} does not replace cobalt ions within the lattice and consequently modify cobalt's oxidation state or electronic environment. Rather, PDF analysis of scattering data shows an unaccounted signal at a radial distance of 3.2–3.5 Å that is distinct from those observed in Co_3O_4, as indicated by the residual signal after fitting to a spinel model (Figures S8B and S8C). This distance is consistent with the La···Co distance in $La_{0.3}CoO_2$ (d(La···Co) = 3.235 Å) where the La^{3+} ion resides between CoO_2 layers.[56] The high positive charge of La^{3+} between the dimensionally reduced $Co(O)_x(OH)_y$ particles, on the order of ~10–70 nm as assessed from DLC and HRTEM imaging, leads to increased stability of the amorphous overlayer. Whereas 0% LaCo operated in acid at pH = 2 is stable for 45 h, 17% LaCo is stable for 80–90 h, after which the catalyst dissolves as indicated by an abrupt increase in overpotential. A similar increase in overpotential

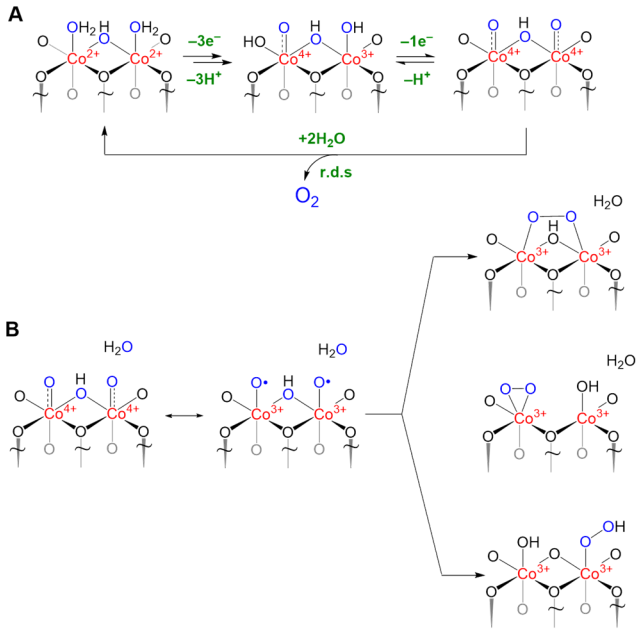

Figure 8. Proposed mechanisms for the oxidation of water to oxygen at the edge sites of $Co(O)_x(OH)_y$ active sites.

is observed after 90 h when similar La^{3+}-cobalt oxide materials are incorporated in PEM electrolyzers (Figure S23 in ref 31). Thus, in the absence of self-healing strategies to stabilize $CoO_x(OH)_y$ active sites,[103−107] the amorphous overlayer ultimately dissolves.

At odds with the predictions of DFT calculations,[30,31] we do not believe that La^{3+} residing at the surface of deconstructed layered cobalt oxide significantly affects the electronic stricture of the cobalt oxide or gives rise to a unique La···Co active site. Rather, the presence of La^{3+} may have a more straightforward role of acting as a Lewis acid resulting in the increase in hydroxylated surface species (Figure 8). In support of this contention, O 1s XPS spectra of LaCo samples show an increase in the concentration of hydroxylated species when compared to the O 1s XPS spectra of the Co_3O_4 spinel lattice (Figure 6). The increase in hydroxylated species precedes the rate-determining step of O–O bond formation in the mechanism displayed in Figure 8. Upon the elimination of O_2, the system returns to the Co^{2+} redox level. This conversion is captured by operando Raman spectra (Figure 4). The A_{1g} mode of Co^{2+} residing in an O_h oxide environment at ~684 cm^{-1} appears during OER operation and subsequently disappears upon the cessation of the OER. Although enhanced spectroscopic signatures of Co^{2+} in in situ and ex situ spectra has led to the assumption of Co^{2+} playing a mechanistic role in OER,[31,108] we believe that its appearance is simply due to an increase in the average concentration of Co^{2+} as a result of its production upon O_2 elimination.

CONCLUSION

Introduction of auxiliary metal ions into first-row metal oxides, particularly those of Co and Ni, can result in significant enhancements of OER activity. Such enhanced OER activity is typically attributed to intrinsic catalytic activity (k_{OER}^0 in eq (1)), leading to the conclusion of superior catalyst design. Indeed, the increased OER performance of first-row metal oxides upon the introduction of lanthanide ions is often ascribed to the introduction of strain into the oxide lattice, or unique electronic properties of Ln···M active sites, though it is known that compositional $LnMO_3$ perovskites undergo decomposition during OER.[109−117] As we show here for La^{3+}, the auxiliary metal promotes the deconstruction of the oxide lattice to hydrous metal oxide particles ($M(O)_x(OH)_y$) with dimensions of nm to as small as metalate clusters. Such lattice deconstruction results in an increased concentration of active sites (C_{as}* in eq (1)), which results in a higher current density at a given overpotential. A signature of this lattice deconstruction is the formation of an amorphous overlayer on the metal oxide. Thus, claims of superior OER catalyst design and claims of the ability to benchmark catalysts[118] must be tempered without knowledge of the nature of the active site and the concentration of these active sites within the overlayer of the crystalline oxide. In this regard, the challenge confronting the rationale design of intrinsically better OER catalysts is the development of new methods to quantify the nature and concentration of active sites.[119] While methods such as underpotential deposition may be used for legacy electrocatalysts such as Pt,[120] it is much more difficult to quantitate the nature and concentration of in situ metal oxide electrocatalysts. Such studies are imperative for guiding the design of truly unique OER catalysts as opposed to enhanced OER performance arising from an increased concentration of active sites.

ASSOCIATED CONTENT

Supporting Information

Details of methods and materials, electrochemical and structural characterizations, spectra and images of 0–17% LaCo films.

AUTHOR INFORMATION

Corresponding Authors

Daniel G. Nocera – Department of Chemistry and Chemical Biology, Harvard University, 12 Oxford Street, Cambridge, MA 02138, United States; orcid.org/0000-0001-5055-320X; E-mail: dnocera@fas.harvard.edu.

Authors

Alaina C. Hartnett – Department of Chemistry and Chemical Biology, Harvard University, 12 Oxford Street, Cambridge, MA 02138, United States; orcid.org/0000-0001-7920-4708.

Ryan J. Evenson – Department of Chemistry and Chemical Biology, Harvard University, 12 Oxford Street, Cambridge, MA 02138, United States; orcid.org/0000-0002-6331-4539.

Agnes E. Thorarinsdottir – Department of Chemistry and Chemical Biology, Harvard University, 12 Oxford Street, Cambridge, MA 02138, United States; orcid.org/0000-0003-2026-5703.

Present Address – Department of Chemistry, University of Rochester, Hutchison Hall, 120 Trustee Road, Rochester, NY 14627, United States.

Samuel S. Veroneau – Department of Chemistry and Chemical Biology, Harvard University, 12 Oxford Street, Cambridge, MA 02138, United States; orcid.org/0000-0003-1491-4172.

Notes

The authors declare no competing financial interests.

ACKNOWLEDGMENTS

This material is based on work supported by the Office of Basic Energy Sciences of the U.S. Department of Energy DE-SC0017619. A.C.H. acknowledges support from the National Science Foundation Graduate Research Fellowship Program (NSF GRFP). This research used beamlines 12-BM, 11-ID-B (or 17-BM, 11-BM) of the Advanced Photon Source, a U.S. Department of Energy Office of Science User Facility operated by Argonne National Laboratory under Contract No. DE-AC02-06CH11357. We acknowledge Daniel R. Morphet for his assistance in performing XAS experiments.

REFERENCES

(1) Segev, G.; Kibsgaard, J.; Hahn, C.; Xu, Z. J.; Cheng, W.-H. (Sophia); Deutsch, T. G.; Xiang, C.; Zhang, J. Z.; Hammarström, L.; Nocera, D. G.; Weber, A. Z.; Agbo, P.; Hisatomi, T.; Osterloh, F. E.; Domen, K.; Abdi, F. F.; Haussener, S.; Miller, D. J.; Ardo, S.; McIntyre, P. C.; Hannappel, T.; Hu, S.; Atwater, H.; Gregoire, J. M.; Ertem, M. Z.; Sharp, I. D.; Choi, K.-S.; Lee, J. S.; Ishitani, O.; Ager, J. W.; Prabhakar, R. R.; Bell, A. T.; Boettcher, S. W.; Vincent, K.; Takanabe, K.; Artero, V.; Napier, R.; Cuenya, B. R.; Koper, M. T. M.; Krol, R. V. D.; Houle, F. The 2022 Solar Fuels Roadmap. *J. Phys. D: Appl. Phys.* **2022**, *55*, 323003.

(2) Peter, S. C. Reduction of CO_2 to Chemicals and Fuels: A Solution to Global Warming and Energy Crisis, *ACS Energy Lett.* **2018**, *3*, 1557–1561.

(3) Cook, T. R.; Dogutan, D. K.; Reece, S. Y.; Surendranath, Y.; Teets, T. S.; Nocera, D. G. Solar Energy Supply and Storage for the Legacy and Nonlegacy Worlds. *Chem. Rev.* **2010**, *110*, 6474–6502.

(4) Lewis, N. S.; Nocera, D. G. Powering the Planet: Chemical Challenges in Solar Energy Utilization. *Proc. Natl. Acad. Sci. U.S.A.* **2006**, *103*, 15729–15735.

(5) Nocera, D. G. Proton-Coupled Electron Transfer: The Engine of Energy Conversion and Storage. *J. Am. Chem. Soc.* **2022**, *144*, 1069–1081.

(6) Eisenberg, R.; Gray, H. B. Preface on Making Oxygen. *Inorg. Chem.* **2008**, *47*, 1697–1699.

(7) Nocera, D. G. Chemistry of Personalized Solar Energy. *Inorg. Chem.* **2009**, *48*, 10001–10017.

(8) Roger, I.; Shipman, M. A.; Symes, M. D. Earth-Abundant Catalysts for Electrochemical and Photoelectrochemical Water Splitting. *Nat. Rev. Chem.* **2017**, *1*, 0003.

(9) Gu, X. K.; Camayang, J. C. A.; Samira, S.; Nikolla, E. Oxygen Evolution Electrocatalysis using Mixed Metal Oxides under Acidic Conditions: Challenges and Opportunities. *J. Catal.* **2020**, *388*, 130–140.

(10) Kim, J. S.; Kim, B.; Kim, H.; Kang, K. Recent Progress on Multimetal Oxide Catalysts for the Oxygen Evolution Reaction *Adv. Energy Mater.* **2018**, *8*, 1702774.

(11) Krivina, R. A.; Ou, Y.; Xu, Q.; Twight, L. P.; Stovall, T. N.; Boettcher, S. W. Oxygen Electrocatalysis on Mixed-Metal Oxides/Oxyhydroxides: From Fundamentals to Membrane Electrolyzer Technology. *Acc. Mater. Res.* **2021**, *2*, 548–558.

(12) Lin, X.; Huang, Y.-C.; Hu, Z.; Li, L.; Zhou, J.; Zhao, Q.; Huang, H.; Sun, J.; Pao, C.-W.; Chang, Y.-C.; Lin, H.-J.; Chen, C.-T.; Dong, C.-L.; Wang, J.-Q.; Zhang, L. 5f Covalency Synergistically Boosting Oxygen Evolution of $UCoO_4$ Catalyst. *J. Am. Chem. Soc.* **2022**, *144*, 416–423.

(13) Yu, Z.-Y.; Duan, Y.; Kong, Y.; Zhang, X.-L.; Feng, X.-Y.; Chen, Y.; Wang, H.; Yu, X.; Ma, T.; Zheng, X.; Zhu, J.; Gao, M.-R.; Yu, S.-H. General Synthesis of Tube-like Nanostructured Perovskite Oxides with Tunable Transition Metal–Oxygen Covalency for Efficient Water Electrooxidation in Neutral Media. *J. Am. Chem. Soc.* **2022** *144*, 13163–13173.

(14) Alkhalifah, M. A.; Howchen, B.; Staddon, J.; Celorrio, V.; Tiwari, D.; Fermin, D. J. Correlating Orbital Composition and Activity of $LaMn_xNi_{1-x}O_3$ Nanostructures toward Oxygen Electrocatalysis. *J. Am. Chem. Soc.* **2022**, *144*, 4439–4447.

(15) Louie; M. W. Bell, A. T. An Investigation of Thin-Film Ni-Fe Oxide Catalysts for the Electrochemical Evolution of Oxygen. *J. Am. Chem. Soc.* **2013**, *135*, 12329–12337.

(16) Suntivich, J.; May, K. J.; Gasteiger, H. A.; Goodenough, J. B.; Shao-Horn, Y. A Perovskite Oxide Optimized for Oxygen Evolution Catalysis from Molecular Orbital Principles. *Science* **2011**, *334*, 1383–1385.

(17) Mu, X.; Wang, K.; Lv, K.; Feng, B.; Yu, X.; Li, L.; Zhang, X.; Yang, X.; Lu, Z. Doping of Cr to Regulate the Valence State of Cu and Co Contributes to Efficient Water Splitting. *ACS Appl. Mater. Interfaces* **2023,** *15*, 16552–16561.

(18) Zhou, D.; Li, F.; Zhao, Y.; Wang, L.; Zou, H.; Shan, Y.; Fu, J.; Ding, Y.; Duan, L.; Liu, M.; Sun, L.; Fan, K. Mechanistic Regulation by Oxygen Vacancies in Structural Evolution Promoting Electrocatalytic Water Oxidation. *ACS Catal.* **2023**, *13,* 4398–4408.

(19) Zhang, R.; Pan, L.; Guo, B.; Huang, Z.-F.; Chen, Z.; Wang, L.; Zhang, X.; Guo, Z.; Xu, W.; Loh, K. P.; Zou, J.-J. Tracking the Role of Defect Types in Co_3O_4 Structural Evolution and Active Motifs during Oxygen Evolution Reaction. *J. Am. Chem. Soc.* **2023**, *145*, 2271–2281.

(20) Jin, L.; Zhang, F.; Gunkel, F.; Wei, X.-K.; Zhang, Y.; Wang, D.; Barthel, J.; Dunin-Borkowski, R. E.; Jia, C.-L. Understanding Structural Incorporation of Oxygen Vacancies in Perovskite Cobaltite Films and Potential Consequences for Electrocatalysis. *Chem. Mater.* **2022**, *34*, 10373–10381.

(21) Alsaç, E. P.; Whittingham, A.; Liu Y.; Smith, R. D. L. Probing the Role of Internalized Geometric Strain on Heterogeneous Electrocatalysis. *Chem. Mater.* **2019**, *31*, 7522–7530.

(22) Smith, R. D. L.; Pasquini, C.; Loos, S.; Chernev, P.; Klingan, K.; Kubella, P.; Mohammadi, M. R.; Gonzalez-Flores D.; Dau, H. Geometric Distortions in Nickel (Oxy)hydroxide Electrocatalysts by Redox Inactive Iron Ions. *Energy Environ. Sci.* **2018**, *11*, 2476–2485.

(23) Petrie, J. R.; Cooper, V. R.; Freeland, J. W.; Meyer, T. L.; Zhang, Z.; Lutterman, D. A.; Lee, H. N. Enhanced Bifunctional Oxygen Catalysis in Strained $LaNiO_3$ Perovskites. *J. Am. Chem. Soc.* **2016**, *138*, 2488–2491.

(24) Bao, J.; Zhang, X.; Fan, B.; Zhang, J.; Zhou, M.; Yang, W.; Hu, X.; Wang, H.; Pan, B.; Xie, Y. Ultrathin Spinel-Structured Nanosheets Rich in Oxygen Deficiencies for Enhanced Electrocatalytic Water Oxidation. *Angew. Chem. Int. Ed.* **2015**, *54*, 7399–7404.

(25) Zhai, Y.; Ren, X.; Wang, B.; Liu, S. High-Entropy Catalyst—A Novel Platform for Electrochemical Water Splitting. *Adv. Funct. Mater.* **2022**, *32*, 2207536.

(26) Abdelhafiz, A.; Wang, B.; Harutyunyan, A. R.; Li, J. Carbothermal Shock Synthesis of High Entropy Oxide Catalysts: Dynamic Structural and Chemical Reconstruction Boosting the Catalytic Activity and Stability toward Oxygen Evolution Reaction. *Adv. Energy Mater.* **2022**, *12*, 2200742.

(27) Li, N.; Bediako, D. K.; Hadt, R. G.; Hayes, D.; Kempa, T. J.; Cube, F. von; Bell, D. C.; Chen, L. X.; Nocera, D. G. Influence of Iron Doping on Tetravalent Nickel Content in Catalytic Oxygen Evolving Films. *Proc. Natl. Acad. Sci. U.S.A.* **2017**, *114*, 1486–1491.

(28) Jain, P.; Jha, S.; Ingole, P. P. Concurrently Engineered Lewis Acid Sites and Coordination Sphere Vacancies in CoFe Prussian Blue Analogues for Boosted Bifunctional Oxygen Electrocatalysis. *ACS Appl. Energy Mater.* **2023**, *6*, 3278–3290.

(29) Wang, Z.-L.; Huang, G.-Y.; Zhu, G.-R.; Hu, H.-C.; Li, C.; Guan, X.-H.; Zhu, H.-B. La-Exacerbated Lattice Distortion of High Entropy Alloys for Enhanced Electrocatalytic Water Splitting. *Appl. Catal. B: Environ. Energy* **2025**, *361*, 124585.

(30) Pan, S.; Li, H.; Wang, T.; Fu, Y.; Wang, S.; Xie, Z.; Wei, L.; Li, H.; Li, N. Er-Doping Enhances the Oxygen Evolution Performance of Cobalt Oxide in Acidic Medium. *ACS Catal.* **2024**, 13814–13824.

(31) Chong, L.; Gao, G.; Wen, J.; Li, H.; Xu, H.; Green, Z.; Sugar, J. D.; Kropf, A. J.; Xu, W.; Lin, X.-M.; Xu, H.; Wang, L.-W.; Liu, D.-J. La- and Mn-Doped Cobalt Spinel Oxygen Evolution Catalyst for Proton Exchange Membrane Electrolysis. *Science* **2023**, *380*, 609–616.

(32) Zhao, Z.; Liu, Y.; Wang, S.; Hu, Z.; Huang, T.; Yu, M.; Chen, X.; Jiang, C.; Liang, Q.; Hu, J. Regulating Electronic Structure of Hollow $La_xCo_yO_4$@NC by La Incorporation for Electrochemical Oxygen Evolution Reaction. *J. Electroanal. Chem.* **2022**, *918*, 116480.

(33) Kim, D.; Yuan, Y.; Suk Lee, L. Y. Electronic Modulation of Cobalt Phosphide by Lanthanum Doping for Efficient Overall Water Splitting in Alkaline Media. *CrystEngComm* **2022**, *24*, 7283–7291.

(34) Xiao, Z.; Zhou, W.; Yang, B.; Liao, C.; Kang, Q.; Chen, G.; Liu, M.; Liu, X.; Ma, R.; Zhang, N. Tuned d-Band States over Lanthanum Doped Nickel Oxide for Efficient Oxygen Evolution Reaction. *Nano Mater. Sci.* **2022**, *5*, 228–236.

(35) Shit, S.; Bolar, S.; Murmu, N. C.; Kuila, T. Minimal Lanthanum-Doping Triggered Enhancement in Bifunctional Water Splitting Activity of Molybdenum Oxide/Sulfide Heterostructure through Structural Evolution. *Chem. Eng. J.* **2022**, *428*, 131131.

(36) Rong, M.; Zhong, H.; Wang, S.; Ma, X.; Cao, Z. La/Ce Doped CoFe Layered Double Hydroxides (LDH) Highly Enhanced Oxygen Evolution Performance of Water Splitting. *Coll. Surf. A: Physicochem. Eng. Aspects* **2021**, *625*, 126896.

(37) Yu, J.; Lu, K.; Wang, C.; Wang, Z.; Fan, C.; Bai, G.; Wang, G.; Yu, F. Modification of NiFe Layered Double Hydroxide by Lanthanum Doping for Boosting Water Splitting. *Electrochim. Acta* **2021**, 390, 138824.

(38) Gileadi, E. *Electrode Kinetics for Chemists, Chemical Engineers, and Materials Scientists*; Wiley-VCH: New York, 1993; Ch 12.2–12.4, pp 109–116.

(39) Gileadi, E. *Physical Electrochemistry, Fundamentals, Techniques and Applications*; Wiley-VCH: Weinheim, 2011, Ch 4.1.2, pp 30–32.

(40) Bard, A. J.; Faulkner, L. R. *Electrochemical Methods: Fundamentals and Applications*, 2nd ed.; John Wiley: New York, 2001; Ch 3.4, pp 98–106.

(41) Surendranath Y.; Nocera, D. G. Oxygen Evolution Reaction Chemistry of Oxide–Based Electrodes. *Prog. Inorg. Chem.* **2012**, *57*, 505–560.

(42) Mondschein, J. S.; Callejas, J. F.; Read, C. G.; Chen, J. Y. C.; Holder, C. F.; Badding, C. K.; Schaak, R. E. Crystalline Cobalt Oxide Films for Sustained Electrocatalytic Oxygen Evolution under Strongly Acidic Conditions. *Chem. Mater.* **2017**, *29*, 950–957.

(43) Lee, S. W.; Carlton, C.; Risch, M.; Surendranath, Y.; Chen, S.; Furutsuki, S.; Yamada, A.; Nocera D. G.; Shao-Horn, Y. The Nature of Lithium Battery Materials under Oxygen Evolution Reaction Conditions. *J. Am. Chem. Soc.* **2012**, *134*, 16959–16962.

(44) Risch, M.; Ringleb, F.; Kohlhoff, M.; Bogdanoff, P.; Chernev, P.; Zaharieva, I.; Dau, H. Water Oxidation by Amorphous Cobalt-Based Oxides: In Situ Tracking of Redox Transitions and Mode of Catalysis. *Energy Environ. Sci.* **2015**, *8*, 661–674.

(45) Bergmann, A.; Martinez-Moreno, E.; Teschner, D.; Chernev, P.; Gliech, M.; Ferreira de Araujo, J.; Reier, T.; Dau H.; Strasser, P. Reversible Amorphization and the Catalytically Active State of Crystalline Co_3O_4 during Oxygen Evolution. *Nat. Commun.* **2015**, *6*, 1.

(46) Gonzalez-Glores, D.; Sanchez, I.; Zaharieva, I.; Klingan, K.; Heidkamp, J.; Chernev, P.; Menezes, P. W.; Driess, M.; Dau H.; Montero, M. L. Heterogeneous Water Oxidation: Surface Activity versus Amorphization Activation in Cobalt Phosphate Catalysts. *Angew. Chem. Int. Ed.* **2015**, *54*, 2472–2476.

(47) Xiaohong, W.; Wei, Q.; Li, L.; Yun, G.; Zhaoyang, X. Photocatalytic Property of Nanostructured Fe^{3+}-Doped Bi_2O_3 Films. *Catal. Commun.* **2009**, *10*, 600–604.

(48) Livage, J.; Henry, M.; Sanchez, C. Sol-Gel Chemistry of Transition Metal Oxides. *Prog. Sol. State Chem.* **1988**, *18*, 259–341.

(49) Biesinger, M. C.; Payne, B. P.; Grosvenor, A. P.; Lau, L. W. M.; Gerson, A. R.; Smart, R. St. C. Resolving Surface Chemical States in XPS Analysis of First Row Transition Metals, Oxides and Hydroxides: Cr, Mn, Fe, Co and Ni. *Appl. Surf. Sci.* **2011**, *257*, 2717–2730.

(50) Li, J. P. H.; Zhou, X.; Pang, Y.; Zhu, L.; I. Vovk, E.; Cong, L.; van Bavel, A. P.; Li, S.; Yang, Y. Understanding of Binding Energy Calibration in XPS of Lanthanum Oxide by in Situ Treatment. *Phys. Chem. Chem. Phys.* **2019**, *21*, 22351–22358.

(51) Stoerzinger, K. A.; Hong, W. T.; Crumlin, E. J.; Bluhm, H.; Biegalski, M. D.; Shao-Horn, Y. Water Reactivity on the $LaCoO_3$ (001) Surface: An Ambient Pressure X-Ray Photoelectron Spectroscopy Study. *J. Phys. Chem. C* **2014**, *118*, 19733–19741.

(52) Picard, J. P.; Baud, G.; Besse, J.P.; Chevalier, R. Croissance Cristalline et Etude Structurale de Co_3O_4. *J. Less Common Met.* **1980**, *75*, 99–104.

(53) Toby, B. H.; Von Dreele, R. B. GSAS-II: The Genesis of a Modern Open-Source All Purpose Crystallography Software Package. *J. Appl. Cryst.* **2013**, *46*, 544–549.

(54) Batchellor, A. S.; Boettcher, S. W. Pulse-Electrodeposited Ni-Fe (Oxy)hydroxide Oxygen Evolution Electrocatalysts with High Geometric and Intrinsic Activities at Large Mass Loadings. *ACS Catal.* **2015**, *5*, 6680–6689.

(55) Bailmare, D. B.; Tripathi, P.; Deshmukh, A. D.; Gupta, B. K. Designing of Two Dimensional Lanthanum Cobalt Hydroxide Engineered High Performance Supercapacitor for Longer Stability under Redox Active Electrolyte. *Sci. Rep.* **2022**, *12*, 3084.

(56) Knížek, K. Hejtmánek, J. Maryško, M. Šantavá, E. Jirák, Z. Buršík, J. Kirakci, K. Beran, P. Structure and Properties of a Novel Cobaltate $La_{0.30}CoO_2$. *J. Sol. State Chem.* **2011**, *184*, 2231–2237.

(57) Swaminathan, J.; Puthirath, A. B.; Sahoo, M. R.; Nayak, S. K.; Costin, G.; Vajtai, R.; Sharifi, T.; Ajayan, P. M. Tuning the Electrocatalytic Activity of Co_3O_4 through Discrete Elemental Doping. *ACS Appl. Mater. Interfaces* **2019**, *11*, 39706–39714.

(58) Liu, Y.-C.; Koza, J. A.; Switzer, J. A. Conversion of Electrodeposited $Co(OH)_2$ to CoOOH and Co_3O_4, and Comparison of Their Catalytic Activity for the Oxygen Evolution Reaction. *Electrochim. Acta* **2014**, *140*, 359–365.

(59) Yang, J.; Liu, H.; Martens, W. N.; Frost, R. L. Synthesis and Characterization of Cobalt Hydroxide, Cobalt Oxyhydroxide, and Cobalt Oxide Nanodiscs. *J. Phys. Chem. C* **2010**, *114*, 111–119.

(60) Campbell, I. H.; Fauchet, P. M. The Effects of Microcrystal Size and Shape on the One Phonon Raman Spectra of Crystalline Semiconductors. *Sol. State Commun.* **1986**, *58*, 739–741.

(61) Koniakhin, S. V.; Utesov, O. I.; Terterov, I. N.; Siklitskaya, A. V.; Yashenkin, A. G.; Solnyshkov, D. Raman Spectra of Crystalline Nanoparticles: Replacement for the Phonon Confinement Model. *J. Phys. Chem. C* **2018**, *122*, 19219–19229.

(62) Utesov, O. I.; Koniakhin, S. V.; Yashenkin, A. G. Effects of Bond Disorder and Surface Amorphization on Optical Phonon Lifetimes and Raman Peak Shape in Crystalline Nanoparticles. *J. Phys. Chem. C* **2021**, *125*, 18444–18455.

(63) Gerken, J. B.; McAlpin, J. G.; Chen, J. Y. C.; Rigsby, M. L.; Casey, W. H.; Britt, R. D.; Stahl, S. S. Electrochemical Water Oxidation with Cobalt-Based Electrocatalysts from pH 0–14: The Thermodynamic Basis for Catalyst Structure, Stability, and Activity. *J. Am. Chem. Soc.* **2011**, *133*, 14431–14442.

(64) Chen, M.; Liu, D.; Qiao, L.; Zhou, P.; Feng, J.; Ng, K. W.; Liu, Q.; Wang, S.; Pan, H. In-Situ/Operando Raman Techniques for in-Depth Understanding on Electrocatalysis. *Chem. Eng. J.* **2023**, *461*, 141939.

(65) Kanan, M. W.; Nocera, D. G. In Situ Formation of an Oxygen-Evolving Catalyst in Neutral Water Containing Phosphate and Co^{2+}. *Science* **2008**, *321*, 1072–1075.

(66) Natarajan, K.; Munirathinam, E.; Yang, T. C. K. Operando Investigation of Structural and Chemical Origin of Co_3O_4 Stability in Acid under Oxygen Evolution Reaction. *ACS Appl. Mater. Interfaces* **2021**, *13*, 27140–27148.

(67) Lee, W. H.; Han, M. H.; Ko, Y.-J.; Min, B. K.; Chae, K. H.; Oh, H.-S. Electrode Reconstruction Strategy for Oxygen Evolution Reaction: Maintaining Fe-CoOOH Phase with Intermediate-Spin State during Electrolysis. *Nat. Commun.* **2022**, *13*, 605.

(68) Rivas-Murias, B.; Salgueiriño, V. Thermodynamic CoO–Co_3O_4 Crossover Using Raman Spectroscopy in Magnetic Octahedron-Shaped Nanocrystals. *J. Raman Spec.* **2017**, *48*, 837–841.

(69) Akimoto, J.; Gotoh, Y.; Oosawa, Y. Synthesis and Structure Refinement of $LiCoO_2$ Single Crystals. *J. Sol. State Chem.* **1998**, *141*, 298–302.

(70) Favaro, M.; Yang, J.; Nappini, S.; Magnano, E.; Toma, F. M.; Crumlin, E. J.; Yano, J.; Sharp, I. D. Understanding the Oxygen Evolution Reaction Mechanism on CoO_x Using Operando Ambient-Pressure X-Ray Photoelectron Spectroscopy. *J. Am. Chem. Soc.* **2017**, *139*, 8960–8970.

(71) Bergmann, A.; Jones, T. E.; Martinez Moreno, E.; Teschner, D.; Chernev, P.; Gliech, M.; Reier, T.; Dau, H.; Strasser, P. Unified Structural Motifs of the Catalytically Active State of Co(Oxyhydr)Oxides during the Electrochemical Oxygen Evolution Reaction. *Nat. Catal.* **2018**, *1*, 711–719.

(72) Huang, Y.-C.; Chen, W.; Xiao, Z.; Hu, Z.; Lu, Y.-R.; Chen, J.-L.; Chen, C.-L.; Lin, H.-J.; Chen, C.-T.; Arul, K. T.; Wang, S.; Dong, C.-L.; Chou, W.-C. *In Situ / Operando* Soft X-Ray Spectroscopic Identification of a Co^{4+} Intermediate in the Oxygen Evolution Reaction of Defective Co_3O_4 Nanosheets. *J. Phys. Chem. Lett.* **2022**, *13*, 8386–8396.

(73) Kang, W.; Wei, R.; Yin, H.; Li, D.; Chen, Z.; Huang, Q.; Zhang, P.; Jing, H.; Wang, X.; Li, C. Unraveling Sequential Oxidation Kinetics and Determining Roles of Multi-Cobalt Active Sites on Co_3O_4 Catalyst for Water Oxidation. *J. Am. Chem. Soc.* **2023**, *145*, 3470–3477.

(74) Jing, C.; Yuan, T.; Li, L.; Li, J.; Qian, Z.; Zhou, J.; Wang, Y.; Xi, S.; Zhang, N.; Lin, H.-J.; Chen, C.-T.; Hu, Z.; Li, D.-W.; Zhang, L.; Wang, J.-Q. Electrocatalyst with Dynamic Formation of the Dual-Active Site from the Dual Pathway Observed by *In Situ* Raman Spectroscopy. *ACS Catal.* **2022**, 12, 10276–10284.

(75) Vitale-Sullivan, M. E.; Chang, A.; Chou, K.-H.; Feng, Z.; Stoerzinger, K. A. Surface Transformations of Electrocatalysts during the Oxygen Evolution Reaction. *Chem. Phys. Rev.* **2023**, *4*, 021309.

(76) Haase, F. T.; Rabe, A.; Schmidt, F.-P.; Herzog, A.; Jeon, H. S.; Frandsen, W.; Narangoda, P. V.; Spanos, I.; Friedel Ortega, K.; Timoshenko, J.; Lunkenbein, T.; Behrens, M.; Bergmann, A.; Schlögl, R.; Roldan Cuenya, B. Role of Nanoscale Inhomogeneities in Co_2FeO_4 Catalysts during the Oxygen Evolution Reaction. *J. Am. Chem. Soc.* **2022** *144*, 12007–12019.

(77) Timoshenko, J.; Haase, F. T.; Saddeler, S.; Rüscher, M.; Jeon, H. S.; Herzog, A.; Hejral, U.; Bergmann, A.; Schulz, S.; Roldan Cuenya, B. Deciphering the Structural and Chemical Transformations of Oxide Catalysts during Oxygen Evolution Reaction Using Quick X-Ray Absorption Spectroscopy and Machine Learning. *J. Am. Chem. Soc.* **2023** *145*, 4065–4080.

(78) Zhang, M.; de Respinis, M.; Frei, H. Time-Resolved Observations of Water Oxidation Intermediates on a Cobalt Oxide Nanoparticle Catalyst. *Nat. Chem.* **2014**, *6*, 362–367.

(79) Kanan, M. W.; Yano, J.; Surendranath, Y.; Dincă, M.; Yachandra, V. K.; Nocera, D. G. Structure and Valency of a Cobalt-Phosphate Water Oxidation Catalyst Determined by in situ X-ray Spectroscopy. *J. Am. Chem. Soc.* **2010**, *132*, 13692–13701.

(80) Du, P.; Kokhan, O.; Chapman, K. W.; Chupas, P. J.; Tiede, D. M. Elucidating the Domain Structure of the Cobalt Oxide Water Splitting Catalyst by X-ray Pair Distribution Function Analysis. *J. Am. Chem. Soc.* **2012**, *134*, 11096–11099.

(81) Farrow, C. L.; Bediako, D. K.; Surendranath, Y.; Nocera, D. G.; Billinge, S. J. L. Intermediate-Range Structure of Self-Assembled Cobalt-Based Oxygen-Evolving Catalyst. *J. Am. Chem. Soc.* **2013**, *135*, 6403–6406.

(82) Kwon, G.; Jang, H.; Lee, J.-S.; Mane, A.; Mandia, D. J.; Soltau, S. R.; Utschig, L. M.; Martinson, A. B. F.; Tiede, D. M.; Kim, H.; Kim J. Resolution of Electronic and Structural Factors Underlying Oxygen-Evolving Performance in Amorphous Cobalt Oxide Catalysts. *J. Am. Chem. Soc.* **2018**, *140*, 10710–10720.

(83) Shin, H.; Xiao H.; Goddard III, W. A. Synergy between Fe and Ni in the Optimal Performance of (Ni,Fe)OOH Catalysts for the Oxygen Evolution Reaction. *Proc. Natl. Acad. Sci. U.S.A.* **2018**, *115*, 5872–5877.

(84) Shin, H.; Xiao H.; Goddard III, W. A. In silico Discovery of New Dopants for Fe-Doped Ni Oxyhydroxide ($Ni_{1-x}Fe_xOOH$) Catalysts for Oxygen Evolution Reaction. *J. Am. Chem. Soc.* **2018**, *140*, 6745–6748.

(85) Winkler, J. R.; Gray, H. B. Electronic Structure of Oxo-Metal Ions in *Structure and Bonding*; Mingos, D. M. P., Day, P., Dahl, J. P., Eds.; Springer: Berlin Heidelberg, 2012; vol. 142; pp 17–28.

(86) Bouvier, M.; Pacheco Bubi, I.; Wiegmann, T.; Qiu, C.; Allongue, P.; Magnussen, O. M.; Maroun, F. Unraveling the Cobalt Oxidation State at the Surface of Epitaxial Cobalt Oxide Films during the Oxygen Evolution Reaction by Operando X-Ray Absorption Spectroscopy/Surface X-Ray Diffraction. *ACS Appl. Energy Mater.* **2023**, *6*, 7335–7345.

(87) Hadt, R. G.; Hayes, D.; Brodsky, C. N.; Ullman, A. M.; Casa, D. M.; Upton, M. H.; Nocera, D. G.; Chen, L. X. X-Ray Spectroscopic Characterization of Co(IV) and Metal–Metal Interactions in Co_4O_4: Electronic Structure Contributions to the Formation of High-Valent States Relevant to the Oxygen Evolution Reaction. *J. Am. Chem. Soc.* **2016**, *138*, 11017–11030.

(88) McAlpin, J. G.; Surendranath, Y.; Dincă, M.; Stich, T. A.; Stoian, S. A.; Casey, W. H.; Nocera, D. G.; Britt, R. D. EPR Evidence for Co(IV) Species Produced During Water Oxidation at Neutral pH. *J. Am. Chem. Soc.* **2010**, *132*, 6882–6883.

(89) Mefford, J. T.; Akbashev, A. R.; Kang, M.; Bentley, C. L.; Gent, W. E.; Deng, H. D.; Alsem, D. H.; Yu, Y.-S.; Salmon, N. J.; Shapiro, D. A.; Unwin, P. R.; Chueh, W. C. Correlative Operando Microscopy of Oxygen Evolution Electrocatalysts. *Nature* **2021**, *593*, 67–73.

(90) Surendranath, Y.; Kanan, M. W.; Nocera, D. G. Mechanistic Studies of the Oxygen Evolution Reaction by a Cobalt–Phosphate Catalyst at Neutral pH. *J. Am. Chem. Soc.* **2010**, *132*, 16501–16509.

(91) Ullman, A. M.; Brodsky, C. N.; Li, N.; Zheng, S.-L.; Nocera, D. G. Probing Edge Site Reactivity of Oxidic Cobalt Water Oxidation Catalysts. *J. Am. Chem. Soc.* **2016**, *138*, 4229–4236.

(92) Koroidov, S.; Anderlund, M. F.; Styring, S.; Thapper, A.; Messinger, J. First Turnover Analysis of Water-Oxidation Catalyzed by Co-Oxide Nanoparticles. *Energy Environ. Sci.* **2015**, *8*, 2492–2503.

(93) Lang, C.; Li, J.; Yang, K. R.; Wang, Y.; He, D.; Thorne, J. E.; Croslow, S.; Dong, Q.; Zhao, Y.; Prostko, G.; Brudvig, G. W.; Batista, V. S.; Waegele, M. M.; Wang, D. Observation of a Potential-Dependent Switch of Water-Oxidation Mechanism on Co-Oxide-Based Catalysts. *Chem* **2021**, *7*, 2101–2117.

(94) Plaisance, C. P.; van Santen, R. A. Structure Sensitivity of the Oxygen Evolution Reaction Catalyzed by Cobalt(II,III) Oxide. *J. Am. Chem. Soc.* **2015**, *137*, 14660–14672.

(95) Nguyen, A. I.; Ziegler, M. S.; Ona-Burgos, P.; Sturzbecher-Hoehne, M.; Kim, W.; Bellone, D. E.; Tilley, T. D. Mechanistic Investigations of

Water Oxidation by a Molecular Cobalt Oxide Analogue: Evidence for a Highly Oxidized Intermediate and Exclusive Terminal Oxo Participation**.** *J. Am. Chem. Soc.* **2015**, *137*, 12865–12872.

(96) Wang, L.-P.; Van Voorhis, T. J. Direct-Coupling O_2 Bond Forming a Pathway in Cobalt Oxide Water Oxidation Catalysts. *Phys. Chem. Lett.* **2011**, *2*, 2200–2204.

(97) Huang, Z.-F.; Song, J.; Du, Y.; Xi, S.; Dou, S.; Nsanzimana, J. M. V.; Wang, C.; Xu, Z. J.; Wang, X. Chemical and Structural Origin of Lattice Oxygen Oxidation in Co–Zn Oxyhydroxide Oxygen Evolution Electrocatalysts. *Nat Energy* **2019**, *4*, 329–338.

(98) Yang, H.; Li, F.; Zhan, S.; Liu,Y; Li, W.; Meng, Q.; Kravchenko, A.; Liu, T.; Yang, Y.; Fang, Y.; Wang, L.; Guan, J.; Furó, I.; Ahlquist, M. S. G.; Sun, L. Intramolecular Hydroxyl Nucleophilic Attack Pathway by a Polymeric Water Oxidation Catalyst with Single Cobalt Sites. *Nat. Catal.* **2022**, *5*, 414–429.

(99) Song, J.; Wei, C.; Huang, Z.-F.; Liu, C.; Zeng, L.; Wang, X.; Xu, Z. J. A Review on Fundamentals for Designing Oxygen Evolution Electrocatalysts. *Chem. Soc. Rev.* **2020**, *49*, 2196–2214.

(100) Reier, T.; Nong, H. N.; Teschner, D.; Schlögl, R.; Strasser, P. Electrocatalytic Oxygen Evolution Reaction in Acidic Environments – Reaction Mechanisms and Catalysts. *Adv. Energy Mater.* **2017**, *7*, 1601275.

(101) Grimaud, A.; Diaz-Morales, O.; Han, B.; Hong, W. T.; Lee, Y.-L.; Giordano, L.; Stoerzinger, K. A.; Koper, M. T. M.; Shao-Horn, Y. Activating Lattice Oxygen Redox Reactions in Metal Oxides to Catalyse Oxygen Evolution. *Nat. Chem.* **2017**, *9*, 457–465.

(102) Lee, S.; Banjac, K.; Lingenfelder M.; Hu, X. Oxygen Isotope Labeling Experiments Reveal Different Reaction Sites for the Oxygen Evolution Reaction on Nickel and Nickel Iron Oxides. *Angew. Chem. Int. Ed.* **2019**, *58*, 10295–10299.

(103) Thorarinsdottir, A. E.; Veroneau, S. V.; Nocera, D. G. Self-Healing Oxygen Evolution Catalysts. *Nat. Commun.* **2022**, *13*, 1243.

(104) Costentin, C.; Nocera, D. G. Self-Healing Catalysis in Water. *Proc. Natl. Acad. Sci. U.S.A.* **2017**, *114*, 13380–13384.

(105) Huynh, M.; Ozel, T.; Liu, C.; Lau, E. C.; Nocera, D. G. Design of Template-Stabilized Active and Earth-Abundant Oxygen Evolution Catalysts in Acid. *Chem. Sci.* **2017**, *8*, 4779–4794.

(106) Huynh, M.; Bediako, D. K.; Nocera, D. G. A Functionally Stable Manganese Oxide Oxygen Evolution Catalyst in Acid. *J. Am. Chem. Soc.* **2014**, *136*, 6002–6010.

(107) Li, N.; Keane, T. P.; Veroneau, S. S.; Hadt, R. G.; Hayes, D.; Chen, L. X.; Nocera, D. G. Template-Stabilized Oxidic Nickel Oxygen Evolution Catalysts. *Proc. Natl. Acad. Sci. U.S.A.* **2020**, *117*, 16187–16192.

(108) Yan, K.-L.; Qin, J.-F.; Lin, J.-H.; Dong, B.; Chi, J.-Q.; Liu, Z.-Z.; Dai, F.-N.; Chai, Y.-M.; Liu, C.-G. Probing the Active Sites of Co_3O_4 for the Acidic Oxygen Evolution Reaction by Modulating the Co^{2+}/Co^{3+} Ratio. *J. Mater. Chem. A* **2018**, *6*, 5678–5686.

(109) Wu, Y.-H.; Janák, M.; Abdala, P. M.; Borca, C. N.; Wach, A.; Kierzkowska, A.; Donat, F.; Huthwelker, T.; Kuznetsov, D. A.; Müller, C. R. Probing Surface Transformations of Lanthanum Nickelate Electrocatalysts during Oxygen Evolution Reaction. *J. Am. Chem. Soc.* **2024**, *146*, 11887–11896.

(110) Dias, J. A.; Andrade Jr, M. A. S.; Santos, H. L. S.; Morelli, M. R.; Mascaro, L. H. Lanthanum-Based Perovskites for Catalytic Oxygen Evolution Reaction. *ChemElectroChem* **2020**, *7*, 3173–3192.

(111) Li, X.; Wang, X.; Ding, J.; Ma, M.; Yuan, S.; Yang, Q.; Wang, Z.; Peng, Y.; Sun, C.; Zhou, H.; Liu, H.; Wu, Y. A.; Huang, K.; Li, L.; Li, G.; Feng, S. Engineering Active Surface Oxygen Sites of Cubic Perovskite Cobalt Oxides toward Catalytic Oxidation Reactions. *ACS Catal.* **2023**, *13*, 6338–6350.

(112) Weber, M. L.; Lole, G.; Kormanyos, A.; Schwiers, A.; Heymann, L.; Speck, F. D.; Meyer, T.; Dittmann, R.; Cherevko, S.; Jooss, C.; Baeumer, C.; Gunkel, F. Atomistic Insights into Activation and Degradation of $La_{0.6}Sr_{0.4}CoO_{3-\delta}$ Electrocatalysts under Oxygen Evolution Conditions. *J. Am. Chem. Soc.* **2022**, *144*, 17966–17979.

(113) Sun, Y.; Wu, C.-R.; Ding, T.-Y.; Gu, J.; Yan, J.-W.; Cheng, J.; Zhang, K. H. L. Direct Observation of the Dynamic Reconstructed Active Phase of Perovskite $LaNiO_3$ for the Oxygen-Evolution Reaction. *Chem. Sci.* **2023**, *14*, 5906–5911.

(114) Baeumer, C.;Li, J.; Lu, Q.; Yu-Lun Liang, A.; Jin, L.; Perin Martins, H.; Duchoň, T.; Glöß, M.; S. M. Gericke; Wohlgemuth, M. A.; Giesen, M.; Penn, E. E.; Dittmann, R.; Gunkel, F.; Waser, R.; Bajdich, M.; Nemšák, S.; Mefford, J. T.; Chueh, W. C.; Tuning Electrochemically Driven Surface Transformation in Atomically Flat $LaNiO_3$ Thin Films for Enhanced Water Electrolysis. *Nat. Mater.* **2021**, *20*, 674–682.

(115) Wu, C.; Wang, X.; Tang, Y.; Zhong, H.; Zhang, X.; Zou, A.; Zhu, J.; Diao, C.; Xi, S.; Xue, J.; Wu, J. Origin of Surface Reconstruction in Lattice Oxygen Oxidation Mechanism Based-Transition Metal Oxides: A Spontaneous Chemical Process. *Angew. Chem. Int. Ed.* **2023**, *62*, e202218599.

(116) Fabbri, E.; Nachtegaal, M.; Binninger, T.; Cheng, X.; Kim, B.-J.; Durst, J.; Bozza, F.; Graule, T.; Schäublin, R.; Wiles, L.; Pertoso, M.; Danilovic, N.; Ayers, K. E.; Schmidt, T. J. Dynamic Surface Self-Reconstruction Is the Key of Highly Active Perovskite Nano-Electrocatalysts for Water Splitting. *Nat. Mater.* **2017**, *16*, 925–931.

(117) May, K. J.; Carlton, C. E.; Stoerzinger, K. A.; Risch, M.; Suntivich, J.; Lee, Y.-L.; Grimaud, A.; Shao-Horn, Y. Influence of Oxygen Evolution during Water Oxidation on the Surface of Perovskite Oxide Catalysts. *J. Phys. Chem. Lett.* **2012**, *3*, 3264–3270.

(118) McCrory, C. C. L.; Jung, S.; Ferrer, I. M.; Chatman, S. M. Peters, J. C.; Jaramillo, T. F.*J. Am.* Chem. *Soc.* **2015**, *137*, 4347–4357.

(119) Liang, C.; Rao, R. R.; Svane, K. L.; Hadden, J. H. L.; Moss, B.; Scott, S. B.; Sachs, M.; Murawski, J.; Frandsen, A. M.; Riley, D. J.; Ryan, M. P.; Rossmeisl, J.; Durrant, J. R.; Stephens, I. E. L. Unravelling the Effects of Active Site Density and Energetics on the Water Oxidation Activity of Iridium Oxides. *Nat. Catal.* **2024**, *7*, 763–775.

(120) Herrero, E.; Buller, L. J.; Abruña, H. D. Underpotential Deposition at Single Crystal Surfaces of Au, Pt, Ag and Other Materials. *Chem. Rev.* **2001**, *101*, 1897–1930.

TOC Graphic